Plasmonic copper sulfide nanoparticles enable dark contrast in optical coherence tomography.

Riccardo Marin, José Lifante, Lucas V. Besteiro, Zhiming Wang, Alexander O. Govorov, Fernando Rivero, Fernando Alfonso, Francisco Sanz-Rodríguez and Daniel Jaque García*

Dr. R. Marin, Prof. D. Jaque García
Fluorescence Imaging Group (FIG), Departamento de Física de Materiales, Facultad de Ciencias, Universidad Autónoma de Madrid, C/ Francisco Tomás y Valiente 7, Madrid 28049, Spain

Mr. J. Lifante, Prof. F. Sanz-Rodríguez, Prof. D. Jaque García
Nanobiology Group, Instituto Ramón y Cajal de Investigación, Sanitaria Hospital Ramón y Cajal, Ctra. De Colmenar Viejo, Km. 9100, 28034 Madrid, Spain

Prof. F. Sanz-Rodríguez
Fluorescence Imaging Group (FIG), Departamento de Biología, Facultad de Ciencias, Universidad Autónoma de Madrid, C/ Francisco Tomás y Valiente 7, Madrid 28049, Spain

Dr. L. V. Besteiro
Institut National de la Recherche Scientifique (INRS), Centre Énergie, Matériaux et Télécommunications, Université du Québec, 1650 Boul. Lionel-Boulet, Varennes, Québec J3X 1S2, Canada

Dr. L. V. Besteiro, Prof. Z. Wang, Prof. A. O. Govorov
Institute of Fundamental and Frontier Sciences, University of Electronic Science and Technology of China, Chengdu 610054, Sichuan, China

Prof. A. O. Govorov
Department of Physics and Astronomy, Ohio University, Athens, OH 45701, USA

Dr. F. Rivero, Dr. F. Alfonso
Unit of Cardiology, Hospital la Princesa, Calle de Diego de León, 62, 28006 Madrid, Spain

E-mail: daniel.jaque@uam.es

ABSTRACT. Optical coherence tomography (OCT) is an imaging technique affording non-invasive optical biopsies. Like for other imaging techniques, the use of dedicated contrast agents helps better discerning biological features of interest during the clinical practice. Although bright OCT contrast agents have been developed, no dark counterpart has been proposed yet. Herein, we report plasmonic copper sulfide nanoparticles as the first OCT dark contrast agents working in the second optical transparency window. These nanoparticles

virtually possess no light scattering capabilities at the OCT working wavelength (approx. 1300 nm); thus, they exclusively absorb the probing light, which in turn results in dark contrast. The small size of the nanoparticles and the absence of apparent cytotoxicity support the amenability of this system to biomedical applications. Importantly, in the pursuit of systems apt to yield OCT dark contrast, we prepared a library of copper sulfide nanoparticles featuring plasmonic resonances spanning the three optical transparency windows, thus highlighting the versatility and potential of these systems in light-controlled biomedical applications.

1. Introduction

Sometimes, the most valuable gifts are those we cannot see with our eyes. As philosophical as it might sound, this sentence well embodies the spirit of the latest research in the field of optical biomedical techniques. With the advancement of our knowledge around the interaction between light and biological tissues, we quickly realized the advantage of moving further down the electromagnetic spectrum and choosing near-infrared (NIR) light over visible.[1-3] The concept of optical transparency windows is now well consolidated and has spurred the development of approaches that make use of specific NIR light to penetrate and probe deeper, with more precision within human tissues. Particularly the second transparency window, also referred to as NIR-II (1000-1400 nm), represents an excellent porthole to peek beneath the skin surface: in fact, it grants an ideal trade-off between reduced scattering, absorption and autofluorescence from tissue components.[2, 4] Embracing these notions, we herein report the first example of dark contrast agent for optical coherence tomography (OCT) working in the NIR-II, leveraging on the plasmonic resonance of noble-metal-free CuS NPs.

OCT is a diagnostic technique that takes advantage of the partial transparency of tissues in the optical transparency windows. It affords optical biopsies of tissues in a fast, non-invasive way.[5-7] These traits make OCT a powerful diagnostic tool, for instance, in ophthalmology,[8, 9] angiography,[10-12] and in the detection of oral carcinomas[13, 14]. The working principle of OCT

2

relies on recording light back-scattered from tissue components at different depths, whose intensity and/or echo time delay are then elaborated to build 2D (B-scans) or 3D images of the investigated area. Although bright contrast agents (i.e., highly-scattering species) are often sought after in order to increase the signal of specific sites of interest,[15, 16] the already bright OCT signals provided by some highly-scattering tissues and tissue interfaces (such as blood-artery wall interface) makes this contrast method impractical in some circumstances. For instance, dark contrast agents could ensure early detection of atheromatous plaques, which nowadays can only be imaged *via* angiography or computed tomography at a relatively advanced stage, when calcification is taking place.[17] Thus, OCT imaging could greatly benefit from dark contrast agents (i.e., strongly absorbing species), which have yet to be reported to the best of our knowledge.

A viable avenue to improve contrast in an OCT scan is to use NPs featuring localized surface plasmon resonance (LSPR) at the probing OCT wavelength.[18, 19] Among plasmonic NPs, gold-based nanostructures are generally the species of choice, because of the possibility to finely tailor their LSPR band over a broad visible-to-NIR range.[20, 21] However, they are costly and architectures above or close to 100 nm have to be prepared to push the LSPR deep into the NIR region, as in the case of high-aspect-ratio gold nanorods (GNRs)[22], gold nanoprisms[15] or gold nanoshells (GNSs).[19] Particles in that size range might undergo a troublesome body clearance– an unwanted side-effect seeking optical imaging. GNSs in particular have been used as bright contrast agents in OCT, owing to the marked scattering component of their light extinction.[18, 19, 23-25] In actuality, it is challenging to prepare small gold nanostructures featuring LSPR with a strong absorption in NIR-II and in the third transparency window (NIR-III; 1500-1870 nm). Copper sulfide in offers the opportunity to complement the toolbox of plasmonic NPs for biomedical applications, easily reaching where gold-based systems have to stretch. Copper sulfide NPs feature a LSPR conveniently centered in the NIR, even when their size is below 10 nm. [26, 27] This translates to an almost complete light absorption, as it minimizes their scattering

efficiency.[28] Because the LSPR arises from the motion of vacancies delocalized in the material's valence band, the spectral position of this feature can be controlled by various means, such as NP size, morphology and stoichiometry (Cu_xS, where x varies from 1 to 2).[29-31] Following this reasoning, capitalizing on the negligible light scattering of small CuS plasmonic NPs, we report on the first example of OCT dark contrast agents operating in NIR-II. These highly-absorbing contrasts agents have properties that are complementary to those of reported highly-scattering species (such as most gold nanostructures), opening new scenarios for OCT imaging that were not conceivable with bright contrast agents – such as atheromata early detection. Importantly, *en route* to these contrast agents, we prepared a library of copper sulfide NPs with variable size, structure and morphology and whose LSPR bands fall in all three optical transparency windows, thus showcasing the versatility of these species in the biomedical context.

2. Results and discussion

Identification of the most promising dark contrast agent.

In the quest for copper sulfide NPs with a plasmonic resonance centered at the working wavelength of the OCT instruments used in this study (1300 and 1320 nm), two different approaches were pursued: *i*) thermolysis of copper complexes in high-boiling-point solvents followed by transfer to aqueous media and *ii*) direct synthesis in water. The results of the syntheses carried out in water are reported in Figure S1 and discussed in the Supporting Information. In fact, the best results in terms of LSPR band spectral position and intensity were obtained following the first approach (Figure S2). Copper sulfide NPs were obtained *via* thermolysis in oleylamine (OLAm) of three different complexes: $Cu(dedtc)_2$, $Cu(tba)_2$, and $Cu(xan)$ (dedtc – diethyldithiocarbamate; tba – thiobenzoate; xan – ethyl xanthate). Infrared absorption spectra of these complexes are reported in Figure S3. The NP growth from $Cu(tba)_2$ and $Cu(xan)$ proceeded in a similar way: initially small plates of hexagonal and triangular

4

morphologies were observed, which then grew into more homogeneously dispersed hexagonal plates. Above 200 °C, larger particles were formed, leading to size distribution broadening. The sample synthesized from $Cu(dedtc)_2$ featured instead larger plates of dissimilar sizes and morphologies already from the first stages of the reaction (Figure S2). This behavior is in line with the observation that, unlike $Cu(dedtc)_2$, $Cu(tba)_2$ and $Cu(xan)$ decompose in the presence of OLAm already at room temperature yielding copper sulfide NPs (Figure S4). The stronger reactivity exhibited by those latter complexes results in faster decomposition kinetics. This leads to the production of a larger number of nuclei and the growth of more, smaller particles. From this pre-screening of the reaction conditions, we identified copper sulfide NPs obtained from the thermolysis of $Cu(tba)_2$ at 200 °C (Figure 1) as the most promising candidates for advancing our study, owing to a good homogeneous size distribution, small size and NIR-II-centered LSPR band. The NPs obtained under those conditions were dispersible in common organic solvents, such as toluene, chloroform and tetrahydrofuran. OLAm molecules on the surface could be easily displaced by thiolated polyethylene glycol (PEG-SH), thus resulting in hydrophilic NPs (Figure 1A). The plate-like NPs were 24.4 and 4.0 nm in diameter and thickness, respectively (Figure 1B). When they were dispersed in water, they featured a hydrodynamic size of approximately 25.2 nm, as obtained from dynamic light scattering (DLS) measurements (Figure 1C). This value was well in accordance with the geometrical size determined from transmission electron microscopy (TEM) observations and suggested the presence of individual, non-aggregated NPs in the dispersion. Importantly, the crystalline structure of the synthesized copper sulfide NPs was covellite, whose stoichiometry is CuS (Figure 1D). This observation is pivotal in this context since, among the several Cu_xS materials, CuS is the one that supports the most intense LSPR. The reason for this is the larger density of empty states in the top of the valence band featured by covellite compared to other stoichiometries where Cu/S > 1.[32]
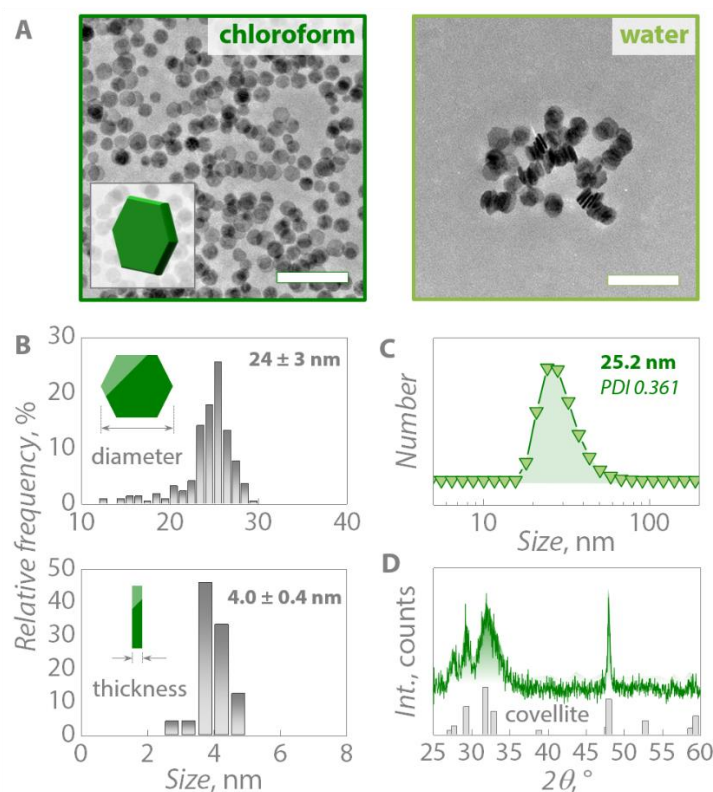
Figure 1. A) TEM images of CuS NPs synthesized at 200 °C from Cu(tba)$_2$, capped with OLAm (dispersed in chloroform) and PEG-SH (dispersed in water). Scale bars are 100 nm. B) Geometrical diameter and thickness of the plate-like CuS NPs as obtained from TEM images. C) Results of DLS measurements performed on a phosphate buffer (1x PB) dispersion of PEG-SH-capped CuS NPs. D) X-ray diffraction (XRD) pattern of the CuS NPs compared to reference covellite pattern (PDF card # 01-078-2121).

Indeed, the synthesized CuS NPs possessed a strong LSPR band, which peaked around 1400 nm–well overlapping with the OCT wavelength used in this study (approx. 1300 nm) (Figure 2A). The contribution at shorter wavelengths (below 500 nm) arises from photon absorption phenomena promoting electrons from the valence to the conduction band of CuS NPs. As expected, the LSPR band experienced a slight bathochromic shift (1396 to 1356 nm) upon transferring the NPs from toluene to water. This is a result of the different refractive index of the solvents ($n_{toluene} = 1.495$, $n_{H_2O} = 1.33$) and the LSPR sensitivity towards this parameter.[26] The calculated extinction profile in water, shown in Figure 2B, is the result of full-wave electrodynamic simulation performed with COMSOL, a commercial finite element method (FEM) software package. The system described in the simulation is a hexagonal CuS

plate (see inset in Figure 2B) immersed in a homogeneous dielectric matrix with a refractive index accounting for the presence of the capping agent (i.e., PEG-SH). The extinction cross section reported in Figure 2B has been averaged over the light's incidence and polarization, to mimic the experimental conditions of a colloidal solution. Results for the longitudinal and transversal plasmonic resonances of the plate can be found in the Supporting Information (Figure S5), alongside all the relevant parameters used in the theoretical model.

These theoretical results highlight a fundamental point: because of the small size of CuS NPs and the relatively large damping rate of the CuS, the extinction coefficient is dominated by the
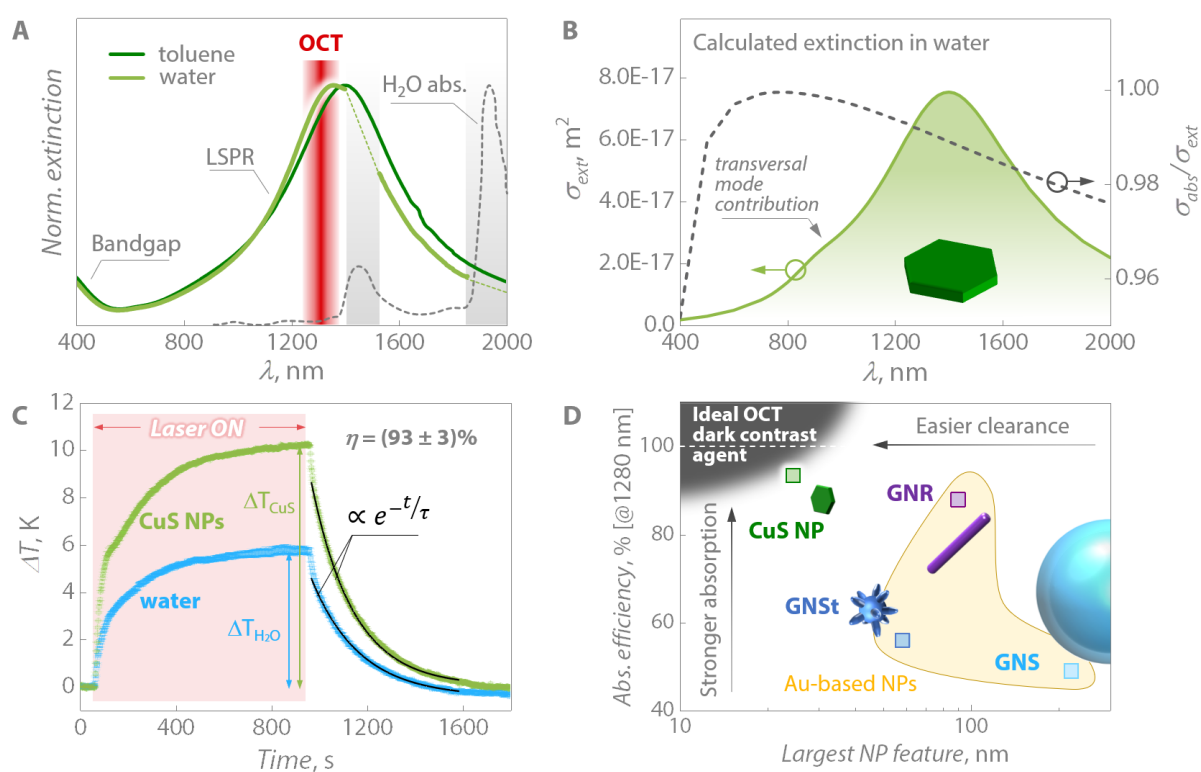

Figure 2. A) Extinction spectra of CuS NPs in toluene (dark green) and in water (light green), respectively before and after exchanging surface OLAm molecules for PEG-SH. Dashed segments in the spectrum of the aqueous dispersion were manually drawn in correspondence of strong water absorption regions. B) Simulated extinction cross section (σ_{ext}) of CuS NPs in water, along with the ratio of absorption (σ_{abs}) over the total extinction (σ_{ext}) that includes both absorption and scattering (σ_{scat}) components. C) Heating-cooling curves obtained from irradiation of water (light blue) and CuS NPs aqueous dispersion (light green) with 1280 nm laser. Black lines in the cooling parts of the curves are single exponential fits to the data. D) Absorption efficiency at 1280 nm (as experimentally calculated) *versus* NP largest feature of plasmonic NPs investigated as OCT contrast agents (GNSt – gold nanostar). The data shown in D was taken from Ref.[18].

7

absorption contribution. The accompanying curves in Figure 2B show that, indeed, at around 1300 nm approximately 99% of the energy of the excited plasmon will be absorbed rather than contribute to scattering.

Providing additional experimental support for this point, the heat conversion efficiency (η) of the system was evaluated under excitation with a 1280 nm laser diode according to an already reported approach (Figure 2C and Figure S6).[18] In fact, considering radiative relaxation pathways negligible, the totality of the absorbed light should be converted to heat. Therefore, under adequate experimental conditions, η provides a fair estimation of the absorption-vs-scattering cross section (σ_{abs} vs σ_{scat}) of the plasmonic NP under study: the closer to 100% the value of this parameter, the more similarly the NPs behave as perfect absorbers. Following the guidelines provided by Roper et al.[33], we calculated η to be $(93 \pm 3)\%$ using the relation:

$$\eta = \frac{Q_{ext} - Q_0}{I(1 - 10^{-OD_\lambda})}$$
Eq. 1

Where Q_{ext} is heat injected into the NP dispersion and Q_0 is the heat dissipated by water. At the denominator is the radiated power extinguished solely by the NPs, which is a function of the total power (I) of the impinging light and the optical density (OD_λ) of the dispersed NPs at the excitation wavelength (*i.e.*, 1280 nm). The heat inputs at the numerators are experimentally determined as a function of the time constants (τ), which are in turn derived from the single exponential fit of the cooling part of the temperature profiles (black lines in Figure 2C). Additional details for η calculations can be found in the Supporting Information.

As we highlighted in a previous study,[28] the methods for the experimental determination of η are usually affected by experimental conditions such as dispersant absorption properties and concentration of the dispersed NPs. Thus, η is really a parameter describing macroscopically the system, rather than providing a picture at the microscopic scale. Hence, it came as no

surprise that the non-negligible absorption of water at 1280 nm (Figure 2A) and an optical path of finite size (approximately 2.8 mm) led to a value of η slightly smaller than the magnitude relating solely to the microscopic properties of the particles (i.e., $\sigma_{abs}/\sigma_{ext}$ ratio).

All in all, the values obtained from simulations and experiment together proved that in these CuS NPs $\sigma_{ext} \cong \sigma_{abs}$. At this point it is important to underscore how, among the plasmonic NPs investigated so far, these CuS NPs are the one that lend themselves best to be used OCT dark contrast agents (Figure 2D). This is because they combine almost exclusive light absorption at the selected NIR wavelength and small size, which are invaluable assets in this framework, allowing for the best imaging performance and subsequent body clearance. In fact, although GNRs might be also effectively yield dark contrast, their high aspect ratio and relatively large size are generally regarded as drawbacks in terms of prolonged residence times, difficult excretion and cytotoxic effects.[34, 35] Not less importantly, the lack of gold in the composition of CuS NPs is another attractive characteristic of the developed system cost-wise.

Cytotoxicity tests.

Aiming for application in biomedical context, the toxicity of the PEG-SH-capped CuS NPs was probed *via* MTT assay[36] (Figure 3). We conducted two different tests, incubating HeLa cells at 4 and 24 h with different concentrations of particles, as already reported in the literature.[37, 38] For the first set of tests, higher concentrations were chosen (from 0.05 to 1.00 mg/mL), which are not expected to persist upon injection of the CuS NPs suspension in the body and its mixing with biological fluids therein present. Concentrations falling in a range more closely mimicking foreseeable *in vivo* conditions were selected for long terms assays (from 0.01 to 1.00 µg/mL). Both set of assays did not show evidence of significant cytotoxicity on the tested cell line, with a maximum decrease of 13% on cell viability at the highest concentration tested (1.00 mg/mL). The results corroborated the amenability of CuS NPs to uses in biological milieus.
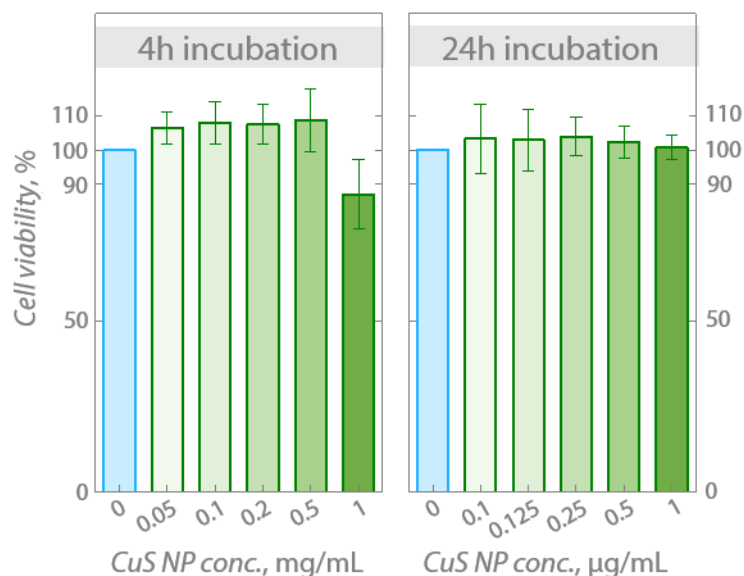
Figure 3. Viability percentage of HeLa cells incubated for 4 and 24 h with dispersions of CuS NPs at different concentrations. Each point corresponds to the mean value (along with its standard deviation) obtained from four different experiments.

Optical coherence tomography imaging.

To prove the aptness of CuS NPs to act as dark OCT contrast agents, we firstly compared the B-scans of Eppendorf tubes filled with dispersions of CuS NPs, GNSs and water (Figure 4). We employed a spectral domain (SD) OCT (Telesto[TM]-II, Thorlabs), with a working wavelength centered at 1300 nm. The bright contrast afforded by the GNSs was in line with the behavior that we previously observed with these same NPs, and followed from the strong scattering of these species at the probing wavelength.[18, 19] The lack of scattering from CuS NPs resulted in the total absence of signal inside the tube, similarly to what was observed for water. Following this experimental observation, we moved to test the usefulness of dark contrast when analyzing highly scattering tissues, such as those high in fat. For this purpose, store-bought pork fat was used (Figure 5). In an excised piece of fat, we laterally injected approximately 15 µL of a 0.4 mg/mL dispersion of CuS NPs in 1x PB (Figure 5A). The injection was executed immediately below the surface (depth < 0.5 mm). This operation was repeated on the same piece of tissue with a 0.05 mg/mL GNSs aqueous dispersion
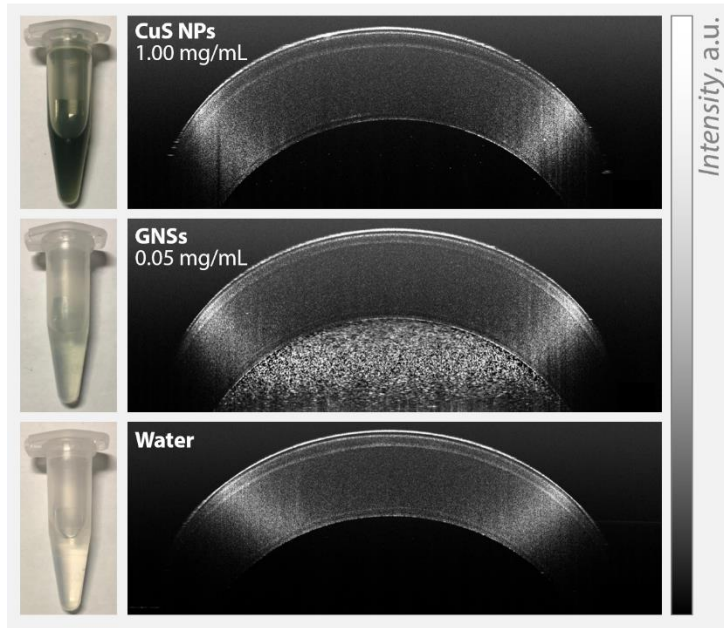
10

Figure 4. OCT B-scans of Eppendorf tubes containing (from top to bottom): dispersion of CuS NPs in 1x PB, aqueous dispersion of GNSs, water.

(Figure 5B), and two OCT scans were performed in correspondence of the areas where the dispersions were injected (Figures 5C and 5D). We selected two regions with a relatively flat surface, in order to ensure that differences in the signal observed below the tissue surface were not stemming from topological variability. It is clear how in correspondence of the area where CuS NPs were injected, the OCT signal sizably decreased compared to the untreated zone (Figure 5C). To assess semi-quantitatively the effect of the presence of the dark contrast agents, we integrated the OCT signal over a rectangular region of interest (ROI) beneath the tissue surface. The results show that the signal decreased approximately 3.6 times in the zone where CuS NPs were injected. The OCT B-scan obtained on the area injected with GNSs was similarly analyzed. Already at a visual inspection, it resulted challenging to identify the region where the GNSs were located (Figure 5D). The integration procedure conducted also for CuS NPs did not allow to discern the signal coming from the GNSs either. Further tests were conducted using a time domain (TD) OCT system for intravascular imaging (Dragonfly[TM] OPTIS[TM] Imaging Catheter, St Jude Medical) equipped with a 1320 nm laser (Figure 5E-G).

11

The catheter was sandwiched between a pristine excised piece of pork fat (top) and one injected with 15 μL of a 0.4 mg/mL CuS NPs suspension (bottom). OCT images were obtained in correspondence of the zones indicated with 1 and 2 in Figure 5E, those being areas of pristine tissue and bearing CuS NPs, respectively. Similarly to what was observed in the SD-OCT images, Figure 5G shows the appearance of a darker area in correspondence of the injected CuS NPs, hence supporting the potential of these particles to be used as OCT dark

Figure 5. Results of the OCT tests conducted using a SD-OCT instrument (A-D) and an OCT instrument for intravascular imaging (E-G). A) Sketch of the approach employed to test the dark contrast abilities of CuS NPs in pork fat, along with a visualization of the mechanism giving rise to dark contrast. B) Picture of the specimen of the imaged pork fat post injection of CuS NPs and GNSs suspensions. C and D) OCT B-scans obtained in correspondence of the areas where the two types of contrast agents were respectively injected, along with the OCT signal intensity derived from the signal integration on the ROIs indicated in the scans. E) Breakdown of the setup employed for the OCT test using a catheter. The red light observed in the catheter is an idle signal used to indicate where the 1320 nm probing light and the rotating mirror are located. The two rectangles labelled 1 (pristine tissue) and 2 (injected CuS NPs) in the middle picture indicate respectively the areas where the OCT images shown in G were recorded. F) Sketch of section indicated in the bottom picture in E, showing how dark contrast is generated. G) OCT images obtained from the two areas highlighted in E. All scale bars (in C, D, and G) are 1 mm.

contrast agents. Importantly, the use of dark contrast agents in intracoronary (IC)-OCT opens the avenue towards molecular imaging of atheromatous plaques, otherwise hardly observable due to their intrinsic bright contrast in OCT scans.

A bigger picture.

The results of this study are expected to spur the research in the field of OCT dark contrast agents, complementing the toolbox of this powerful, non-invasive diagnostic approach. In fact, we are not suggesting that the use of dark contrast agents would be a better way to visualize features of interest in biological tissues broadly speaking. It is known, for instance, that breast cancer cells might appear already darker than the tissues around them in OCT images.[39] Hence, dark contrast would not be beneficial in this situation. Also, many OCT-based techniques make use of the backscattered light, extracting information not only from its intensity but also from, *e.g.*, its phase and polarization. In those cases, already proposed gold-based plasmonic particles, such as high-aspect ratio GNRs and GNSs, are the contrast agents of choice, since they possess unrivalled light scattering capabilities in the optical transparency windows (NIR-I and NIR-II above all). Nonetheless, as mentioned above, imaging of atheromata is one of the foreseeable applications where CuS NPs could provide undeniable advantage over bright contrast agents. The next steps in this direction would be to modify the surface of CuS NPs with targeting moieties promoting selective accumulation at lipid-rich sites on the artery wall. Assessment of the state of atheromateous plaques at an early stage would therefore become possible, with tremendous benefits in terms of prevention of coronary diseases. More in general, highly scattering tissues, which naturally appear bright in OCT images, could be expected to be better investigates using highly absorbing (rather than highly scattering) contrast agents.

Going one step further, the data herein reported has an even broader appeal. *En route* to CuS NPs suitable to act as dark contrast agents, we uncovered the full arsenal of potential of NIR-absorbing plasmonic copper sulfide NPs. This is appreciable from the reported extinction spectra of selected Cu_xS NPs (Figure 6). The attractiveness of these systems resides in the

13

possibility to cover an incredibly broad wavelength range in the NIR, which encompass all three transparency windows, i.e., NIR-I (750-950 nm), NIR-II (1000-1400 nm) and NIR-III (1500-1870 nm). Size, morphology and crystal structure/stoichiometry are the parameters governing the plasmonic properties of these systems. Careful selection of reaction conditions and precursors grants the control over those parameters, thus making it possible to tailor the properties of the plasmonic copper sulfide NPs to the needs of the application sought after. For instance, the high heat conversion efficiency measured for the investigated CuS NPs makes them ideal also in the context of photothermal therapy in NIR-II. Small covellite NPs (light green) where obtained directly in water using citrate molecules as capping agents, using a modified reported approach.[40] They showed a LSPR band mainly centered in NIR-I, while hydrophilic copper sulfide NPs obtained in the presence of acetylacetonate featured an absorption falling prominently within NIR-II (dark brown). The attribution to yarrowite crystal structure was supported by elemental analysis performed on this sample, which returned a Cu/S ratio of 1.15 ± 0.03, compatible with that of yarrowite (1.125). Stunningly, absorption in NIR-III could be easily achieved with copper sulfide NPs derived through the already reported thermolysis of copper thiocyanate (CuSCN) in OLAm,[41] and subsequent transfer to water following the same procedure adopted for CuS NPs (light brown). Given the relatively small size of these particles, the LSPR band of this sample is also expected to have an almost purely absorptive behavior. Because of these properties, these particles may conceivably perform as OCT dark contrast agents for instruments working at 1700 nm.[42] Clearly, other imaging techniques relying on light as a probing mean such as photoacoustic imaging,[43] could greatly benefit from the use of this gamut of small, NIR-absorbing NPs. Moreover, the incorporation of the ^{64}Cu reactive isotope in copper sulfide NPs enables their use in positron-emission tomography, thus opening the door to the preparation of multifunctional biological labels for the accurate localization of diseased tissues.
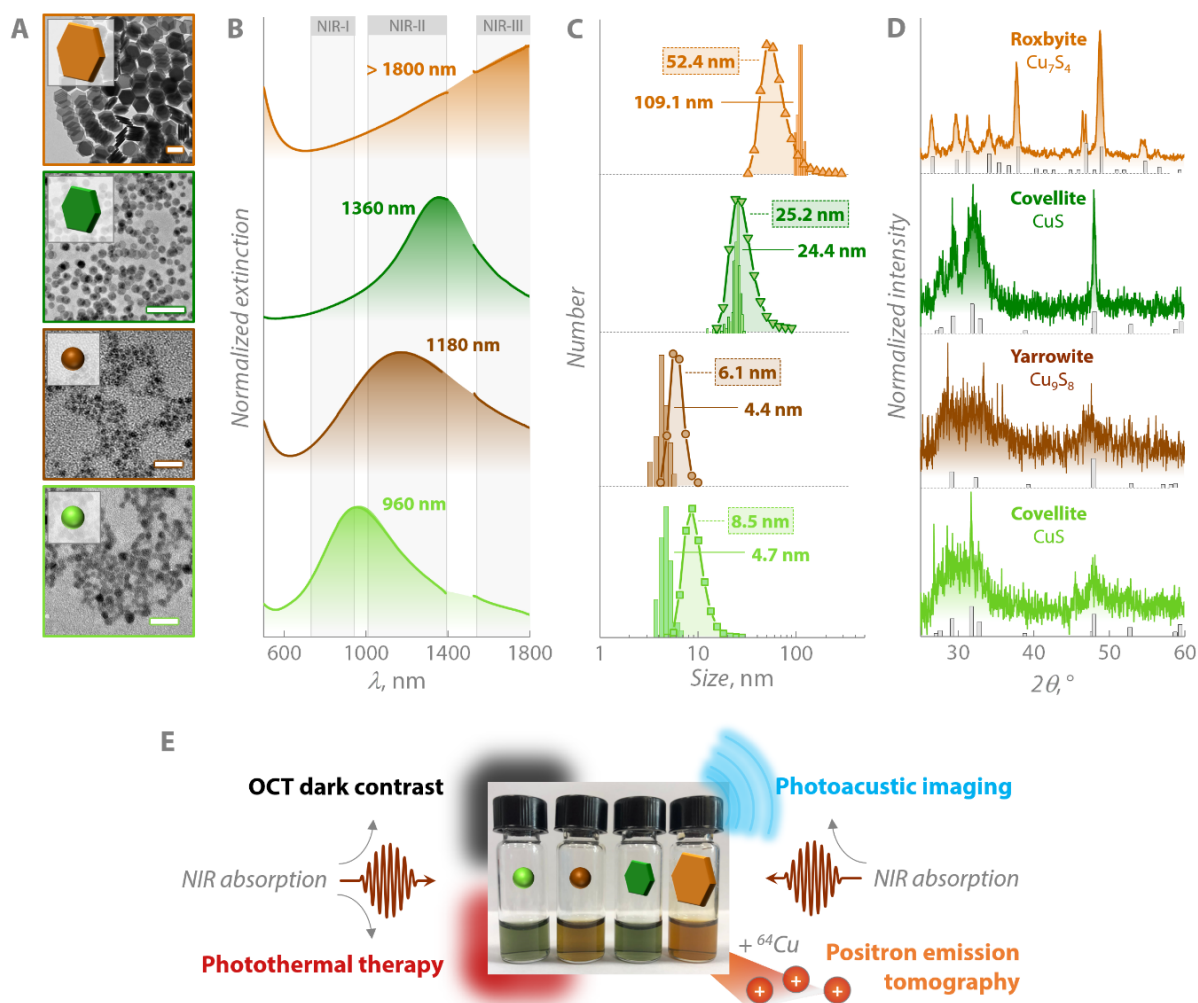
14

Figure 6. TEM images (A), extinction spectra (B), geometrical and hydrodynamic size (C), and X-ray diffraction patterns (D) of the copper sulfide NPs synthesized in the quest for OCT dark contrast agents. Scale bars in A are 100 and 20 nm for the two top and the two bottom TEM images. In C, the geometrical size reported is the largest NP's feature (i.e., for plate-like particles, the thickness is not reported). The reference patterns in D are taken from PDF # 01-078-2121 (covellite), # 00-036-0379 (yarrowite), # 00-023-0958 (roxbyite). In E, some of the possible applications of copper sulfide NPs in the biomedical context are presented.

3. Conclusion

We herein reported the first example of optical coherence tomography (OCT) dark contrast agent, in the form of plasmonic copper sulfide nanoparticles working in the second optical transparency window. The synthesized nanoparticles featured the optimal characteristics for OCT dark contrast agents: small size, no observed cytotoxicity and negligible light scattering at the working wavelengths of the employed OCT instruments–which worked respectively in spectral- and time-domain. Importantly, in the quest for nanoparticles apt for that use, we

15

developed a full library of copper sulfide nanoparticles with small size and plasmonic resonance bands covering all three optical transparency windows. Overall, the results we herein reported not only show the possibility of achieving dark contrast in OCT, thus expectedly encouraging the research towards the improvement and development of novel such contrast agents. Even more importantly, from a broader perspective, we point out the remarkable potential of these systems, which has yet to be completely harnessed in the biomedical context.

4. Experimental

Chemicals.

Sodium diethyldithiocarbamate trihydrate (Na(dedtc)·$3H_2O$, 98%, Alfa Aesar), thiobenzoic acid (Htba, 90%, Acros Organics), potassium ethyl xanthate (K(xan), 97+%, Acros Organics), potassium carbonate (K_2CO_3, Fisher), copper chloride dihydrate ($CuCl_2 \cdot 2H_2O$, 99%, Alfa Aesar), copper thiocyanate (CuSCN, 96%, Alfa Aesar), mercaptopropionic acid (MPA, 99%, Alfa Aesar), trisodium citrate (Na_3(cit), 98%, Acros Organics), mercapto hexadecanoic acid (MHDA, 90%, Aldrich), acetyl acetone (Hacac, 99.5%, Riedel-de-Haën), ethyldiaminotetracetic acid (H_4EDTA, 99%, Acros Organics), glutathione reduced (GSH, 98+%, Alfa Aesar), sodium sulfide nonahydrate ($Na_2S \cdot 9H_2O$, 98%, Alfa Aesar), polyethylene glycol thiol (PEG-SH, MW = 2000, Aldrich), oleyl amine (OLAm, 80-90%, Acros Organics), chloroform (CLF, Fisher), tetrahydrofuran (THF, Fisher), isopropanol (iPrOH, Fisher) were used as received.

Synthesis of copper complexes.

All the syntheses were carried out under ambient conditions. The synthesis of copper sulfide NPs in aqueous environment and from CuSCN are reported in the Supporting Information. Among the synthesized complexes, Cu(dedtc)$_2$ is very soluble in a variety of organic solvents (chloroform, dichloromethane, acetone), Cu(xan) is only sparingly soluble in chloroform, while Cu(tba)$_2$ was insoluble in all tested solvents.

Cu(dedtc)$_2$. To 20 mL of a 0.2 M aqueous solution of Na(dedtc), 5 mL of a 0.4 M aqueous solution CuCl$_2$·2H$_2$O were added dropwise. A dark brown appeared immediately. The mixture was left under stirring for 20 min. The precipitate was collected, washed three times with water and dried overnight under vacuum at room temperature. The dark brown complex was stored in a desiccator. Elemental analysis. Calcd.: C 33.4%, H 5.6%, N 7.8%, S 35.6%. Exp.: C 33.0(2)%, H 5.6(1)%, N 7.6(1)%, S 33.5(2)%.

Cu(xan). To 10 mL of a 0.2 M aqueous solution of K(xan), 5 mL of a 0.4 M aqueous solution CuCl$_2$·2H$_2$O were added dropwise. A yellow precipitate formed immediately and became slightly darker in color over the course of 30 min. The precipitate was collected, washed three times with water and dried overnight under vacuum at room temperature in the dark. The bright yellow complex was stored in a desiccator and wrapped in aluminum foil to avoid possible UV-prompted decomposition. Calcd.: C 19.5%, H 2.7%, S 34.7%. Exp.: C 19.4(1)%, H 2.8(1)%, S 33.3(2)%.

Cu(tba)$_2$. K(tba) was prepared adding 5 mL of Htba (64.2 mmol) to 100 mL of a stirring solution of 4.4 g (32.1 mmol) of K$_2$CO$_3$ in 100 mL of water. The yellow solution was stirred for 2 h and the water was then removed with the aid of a rotary evaporator. The beige precipitate was collected, re-dissolved in 50 mL of water, filtered and dried again. K(tba) was collected as a beige powder and used without further purification. For the synthesis of the copper complex, to 10 mL of a 0.4 M aqueous solution of K(tba), 5 mL of a 0.4 M aqueous solution CuCl$_2$·2H$_2$O were added dropwise. A yellow precipitate formed immediately, which turned orange upon stirring over the course of 2 h. The precipitate was collected, washed three times with water and dried overnight under vacuum at room temperature in the dark. The bright orange complex was stored in a desiccator and wrapped in aluminum foil to avoid possible UV-prompted decomposition. Calcd.: C 49.8%, H 3.0%, S 19.0%. Exp.: C 47.9(1)%, H 3.1(1)%, S 17.7(1)%.

Synthesis of copper sulfide NPs from copper complexes.

The synthesis of copper sulfide NPs from the thermolysis of the prepared copper complexes were carried out in the same way. 30 mg of the chosen complex were introduced in a 50-mL three-neck round-bottom flask along with 10 mL of OLAm. The solution was degassed at 90 °C for 30 min and then the flask was then purged with N_2. The temperature was set to 220 °C and aliquots were sampled at different temperatures as well as at different time marks after reaching the set temperature. All the aliquots were quenched in toluene and the NPs precipitated adding acetone. The particles were collected through centrifugation (30,000 rcf, 10 min) and finally re-dispersed in toluene for optical characterization. For TEM observations, the particles were diluted in chloroform.

To synthesize the CuS NPs used in the study, the same procedure outlined above was followed but, upon reaching 200 °C, the reaction mixture was rapidly quenched to room temperature. Three mL of toluene were added to the crude reaction product, followed by the addition of 30 mL of acetone and centrifugation at 3,820 rcf for 10 min. The particles were then re-dispersed in toluene and precipitated with acetone 3 more times. The particles were stored in 5 mL of toluene at 5 °C.

Transfer of CuS NPs to water.

The hydrophobic CuS NPs were transferred to water and made biocompatible upon exchanging the OLAm molecules on the surface for PEG-SH. In a typical procedure, 500 μL of the CuS NPs toluene suspension were precipitated with acetone, recovered upon centrifugation and re-dispersed in 250 μL of THF. 10 mg of PEG-SH were added to the suspension, followed by 1 mL of water. The mixture was sonicated for 30 s and vortexed for 1 min. Finally, it was stirred at 70 °C to evaporate the THF. Upon cooling, the exchanged OLAm crushed out of solution. The suspension in water was centrifuged at 30,000 rcf for 5 min and the solid discarded. The aqueous suspension of CuS NPs was diluted to 2 mL with water (or the desired buffer) and filtered through a 0.45 μm syringe filter. This procedure yielded an optically clear suspension which was further characterized and used for OCT experiments. In case of loss of colloidal

stability of the suspension, few milligrams of PEG-SH were added, followed by addition of excess iPrOH, centrifuged at 30,000 *rcf* at 4 °C for 45 min and re-dispersed in the desired aqueous medium.

Physicochemical characterization.

The NPs were imaged on carbon-coated copper grids using a JEM1400 Flas (JEOL) microscope operating at 100 kV acceleration voltage. The size of the nanoparticles was estimated from the TEM images, counting at least 200 NPs using ImageJ software. The hydrodynamic size was obtained at 25°C, using a Malvern Zetasizer Nano ZS90 (Malvern) with a detection angle of 173° and an equilibration time of 120 s. The optical extinction spectra were recorded at room temperature with an UV/VIS/NIR spectrophotometer (Perkin Elmer Lambda1050) using a 4-nm step. Infrared spectra were obtained in transmission mode on a Spectrum Two instrument (Perkin Elmer) in the 450-4000 cm^{-1} range with 4 cm^{-1} resolution, preparing KBr tablets containing 1%wt of the analyzed material. Elemental analysis of the metal complexes was carried out on a CHNS-932 (LECO) elemental analyzer using 1 mg of sample, using the Dumas method, which is based on a direct oxidative combustion of the sample at 1000 °C. The composition of copper sulfide NPs synthesized in the presence of acetylacetone was assessed using a total X-ray fluorescence (TXRF) instrument S2 PICOFOX (Bruker).

Heat conversion efficiency determination.

The light-to-heat transduction capability of the CuS NPs was evaluated according to a method reported in the literature. The set-up is sketched in the Supporting Information (Figure S6). Two wells of a 24-well plate were filled with 500 µL of de-ionized water and an aqueous dispersion of CuS NPs. Both liquids will be referred to as sample in this context. The sample was irradiated with a 1280-nm fiber-coupled laser and the temperature was registered using a E40bx infrared thermal camera (FLIR), controlled through the built-in software. The heating-cooling curves

were directly derived from the live images recorded using the thermal camera and the total power of the excitation light was measured before the sample with the aid of a power-meter. The acquisition of the heating-cooling curves was performed three times for water and CuS NPs respectively.

Cytotoxicity tests.

The HeLa human cervical epithelial cell line was grown in Dulbecco's Modified Eagle's Medium (DMEM, Gibco, Paisley, Scot- land, UK) supplemented with fetal calf serum (FCS 10%, Gibco) and 0.5% of antibiotics (penicillin G [10,000 U/mL] and streptomycin sulfate [10,000 mg/mL] (Gibco)). Cells were grown in a Thermo Scientific Midi 40 CO2 Incubator (Thermo Fisher Scientific Inc.) with a 5% CO_2 atmosphere, a 95% relative humidity and a constant temperature of 37 ℃.

The viability of HeLa cells exposed to CuS NPs was analyzed by the MTT assay[36]. Twenty-four hours after appropriate treatments with CuS NPs, 3-(4,5-dimethylthiazol-2-yl)-2,5-diphenyltetrazolium bromide (MTT) solution was added to each well at a concentration of 0.5 ng/mL, and plates were incubated at 37 ℃ for 2 h. The resulting formazan crystals were dissolved by the addition of DMSO and absorbance was measured at 540 nm. Cell viability was estimated as a percentage relative to the mean absorption obtained from control cells (not incubated with the CuS NPs; 100% viability).

OCT measurements.

OCT measurements were conducted using two different instruments: one working in spectral-domain (SD) and one in time-domain (TD). The former is a Thorlabs Telesto OG-1300 with a maximum working wavelength of 1300 nm (range 1250-1380 nm), mounting a LSM03 scan lens with a working distance of 25.1 mm, having an axial scan rate of up to 92 kHz and axial resolution in water of 4.9 μm, with a maximum imaging depth of 2.5 mm. The latter is a commercially available OPTIS™ OCT Imaging System for intravascular imaging equipped

with a Dragonfly™ OPTIS™ Imaging Catheter (St Jude Medical/Abbott) used in clinical

practice, with a working wavelength of 1320 nm, an axial scan rate of up to 90 kHz and axial

resolution in tissue of 15 μm, with a maximum imaging depth of 3 mm. For both experiments,

store-bought pork fat was used as model tissue where the contrast agents were injected.

References

[1]   E. Hemmer, A. Benayas, F. Légaré, F. Vetrone, *Nanoscale Horiz.* **2016**, *1*, 168.
[2]   B. del Rosal, A. Benayas, *Small Methods* **2018**, *2*, 1800075.
[3]   A. Skripka, A. Benayas, R. Marin, P. Canton, E. Hemmer, F. Vetrone, *Nanoscale* **2017**, *9*, 3079.
[4]   Kenry, Y. Duan, B. Liu, *Adv. Mater.* **2018**, *30*, e1802394.
[5]   M. Adhi, J. S. Duker, *Curr. Opin. Ophthalm.* **2013**, *24*, 213.
[6]   D. Thomas, G. Duguid, *Eye* **2004**, *18*, 561.
[7]   A. G. Podoleanu, *Br. J. Radiol.* **2005**, *78*, 976.
[8]   M. A. Ibrahim, Y. J. Sepah, R. C. A. Symons, R. Channa, E. Hatef, A. Khwaja, M. Bittencourt, J. Heo, D. V. Do, Q. D. Nguyen, *Eye* **2011**, 26, 454.
[9]   M. Lapierre-Landry, A. Y. Gordon, J. S. Penn, M. C. Skala, *Sci. Rep.* **2017**, *7*, 9228.
[10]   T. Kume, S. Uemura, *Cardiovasc. Interv. Ther.* **2017**, *33*, 1.
[11]   J. Hu, T. Gorsak, E. Martín Rodríguez, D. Calle, T. Muñoz‑Ortiz, D. Jaque, N. Fernández, L. Cussó, F. Rivero, R. Aguilar Torres, J. García Solé, A. Mertelj, D. Makovec, M. Desco, D. Lisjak, F. Alfonso, F. Sanz‑Rodríguez, D. H. Ortgies, *ChemPhotoChem* **2019**, *3*, 529.
[12]   J. Hu, D. H. Ortgies, E. Martín Rodríguez, F. Rivero, R. Aguilar Torres, F. Alfonso, N. Fernández, G. Carreño-Tarragona, L. Monge, F. Sanz-Rodriguez, M. d. C. Iglesias, M. Granado, A. L. García-Villalon, J. García Solé, D. Jaque, *Adv. Opt. Mater.* **2018**, *6*, 1800626.

[13] C.-K. Lee, T.-T. Chi, C.-T. Wu, M.-T. Tsai, C.-P. Chiang, C.-C. Yang, *Biomed. Opt. Express* **2012**, *3*, 1632.

[14] Z. Hamdoon, W. Jerjes, G. McKenzie, A. Jay, C. Hopper, *Photodiagnosis Photodyn. Ther.* **2016**, *13*, 211.

[15] P. Si, E. Yuan, O. Liba, Y. Winetraub, S. Yousefi, E. D. SoRelle, D. W. Yecies, R. Dutta, A. de la Zerda, *ACS Nano* **2018**, *12*, 11986.

[16] T. M. Lee, A. L. Oldenburg, S. Sitafalwalla, D. L. Marks, W. Luo, F. J. Toublan, K. S. Suslick, S. A. Boppart, *Opt. Lett.* **2003**, *28*, 1546.

[17] M. Kolossvary, B. Szilveszter, I. F. Edes, S. Nardai, V. Voros, I. Hartyanszky, B. Merkely, S. Voros, P. Maurovich-Horvat, *Am. J. Cardiol.* **2016**, *117*, 1863.

[18] J. Hu, D. Romero Abujetas, D. Tsoutsi, L. Leggio, F. Rivero, E. Martín Rodríguez, R. Aguilar Torres, J. A. Sánchez-Gil, H. Loro Ramírez, D. Gallego, H. Lamela Rivera, P. Rivera Gil, F. Alfonso, J. García Solé, D. Jaque, *APL Photonics* **2018**, *3*, 080803.

[19] J. Hu, F. Sanz-Rodríguez, F. Rivero, E. M. Rodríguez, R. A. Torres, D. H. Ortgies, J. G. Solé, F. Alfonso, D. Jaque, *Nano Res.* **2017**, *11*, 676.

[20] J. Perezjuste, I. Pastorizasantos, L. Lizmarzan, P. Mulvaney, *Coord. Chem. Rev.* **2005**, *249*, 1870.

[21] E. C. Dreaden, A. M. Alkilany, X. Huang, C. J. Murphy, M. A. El-Sayed, *Chem. Soc. Rev.* **2012**, *41*, 2740.

[22] O. Liba, E. D. SoRelle, D. Sen, A. de la Zerda, *Sci. Rep.* **2016**, *6*, 23337.

[23] C. Zhou, T. H. Tsai, D. C. Adler, H. C. Lee, D. W. Cohen, A. Mondelblatt, Y. Wang, J. L. Connolly, J. G. Fujimoto, *Opt. Lett.* **2010**, *35*, 700.

[24] A. Agrawal, S. Huang, A. Wei Haw Lin, M. H. Lee, J. K. Barton, R. A. Drezek, T. J. Pfefer, *J. Biomed. Opt.* **2006**, *11*, 041121.

[25] E. V. Zagaynova, M. V. Shirmanova, M. Y. Kirillin, B. N. Khlebtsov, A. G. Orlova, I. V. Balalaeva, M. A. Sirotkina, M. L. Bugrova, P. D. Agrba, V. A. Kamensky, *Phys. Med. Biol.* **2008**, *53*, 4995.

[26] J. M. Luther, P. K. Jain, T. Ewers, A. P. Alivisatos, *Nat. Mater.* **2011**, *10*, 361.

[27] P. L. Saldanha, R. Brescia, M. Prato, H. Li, M. Povia, L. Manna, V. Lesnyak, *Chem. Mater.* **2014**, *26*, 1442.

[28] R. Marin, A. Skripka, L. V. Besteiro, A. Benayas, Z. Wang, A. O. Govorov, P. Canton, F. Vetrone, *Small* **2018**, *14*, e1803282.

[29] Y. Xie, A. Riedinger, M. Prato, A. Casu, A. Genovese, P. Guardia, S. Sottini, C. Sangregorio, K. Miszta, S. Ghosh, T. Pellegrino, L. Manna, *J. Am. Chem. Soc.* **2013**, *135*, 17630.

[30] Y. Xie, G. Bertoni, A. Riedinger, A. Sathya, M. Prato, S. Marras, R. Tu, T. Pellegrino, L. Manna, *Chem. Mater.* **2015**, *27*, 7531.

[31] P. Roy, S. K. Srivastava, *CrystEngComm* **2015**, *17*, 7801.

[32] A. Comin, L. Manna, *Chem. Soc. Rev.* **2014**, *43*, 3957.

[33] D. K. Roper, W. Ahn, M. Hoepfner, *J. Phys. Chem. C* **2007**, *111*, 3636.

[34] S. Barua, S. Mitragotri, *Nano Today* **2014**, *9*, 223.

[35] H. Chen, W. Zhang, G. Zhu, J. Xie, X. Chen, *Nat. Rev. Mater.* **2017**, *2*, 17024.

[36] T. L. Riss, R. A. Moravec, A. L. Niles, S. Duellman, H. A. Benink, T. J. Worzella, L. Minor, in *Assay Guidance Manual* (Eds: G. S. Sittampalam, A. Grossman, K. Brimacombe, M. Arkin, D. Auld, C. Austin, J. Baell, B. Bejcek, J. M. M. Caaveiro, T. D. Y. Chung, N. P. Coussens, J. L. Dahlin, V. Devanaryan, T. L. Foley, M. Glicksman, M. D. Hall, J. V. Haas, S. R. J. Hoare, J. Inglese, P. W. Iversen, S. D. Kahl, S. C. Kales, S. Kirshner, M. Lal-Nag, Z. Li, J. McGee, O. McManus, T. Riss, O. J. Trask, Jr., J. R. Weidner, M. J. Wildey, M. Xia, X. Xu), Eli Lilly & Company and the National Center for Advancing Translational Sciences, Bethesda (MD) **2004**.

[37]   Y. Li, W. Lu, Q. Huang, M. Huang, C. Li, W. Chen, *Nanomedicine (Lond)* **2010**, *5*, 1161.

[38]   W. Feng, W. Nie, Y. Cheng, X. Zhou, L. Chen, K. Qiu, Z. Chen, M. Zhu, C. He, *Nanomedicine* **2015**, *11*, 901.

[39]   O. Assayag, M. Antoine, B. Sigal-Zafrani, M. Riben, F. Harms, A. Burcheri, K. Grieve, E. Dalimier, B. Le Conte de Poly, C. Boccara, *Technol. Cancer Res. Treat.* **2014**, *13*, 455.

[40]   W. Gao, Y. Sun, M. Cai, Y. Zhao, W. Cao, Z. Liu, G. Cui, B. Tang, *Nat. Commun.* **2018**, *9*, 231.

[41]   S. Lee, S. Baek, J. P. Park, J. H. Park, D. Y. Hwang, S. K. Kwak, S.-W. Kim, *Chem. Mater.* **2016**, *28*, 3337.

[42]   M. Yamanaka, T. Teranishi, H. Kawagoe, N. Nishizawa, *Sci. Rep.* **2016**, *6*, 31715.

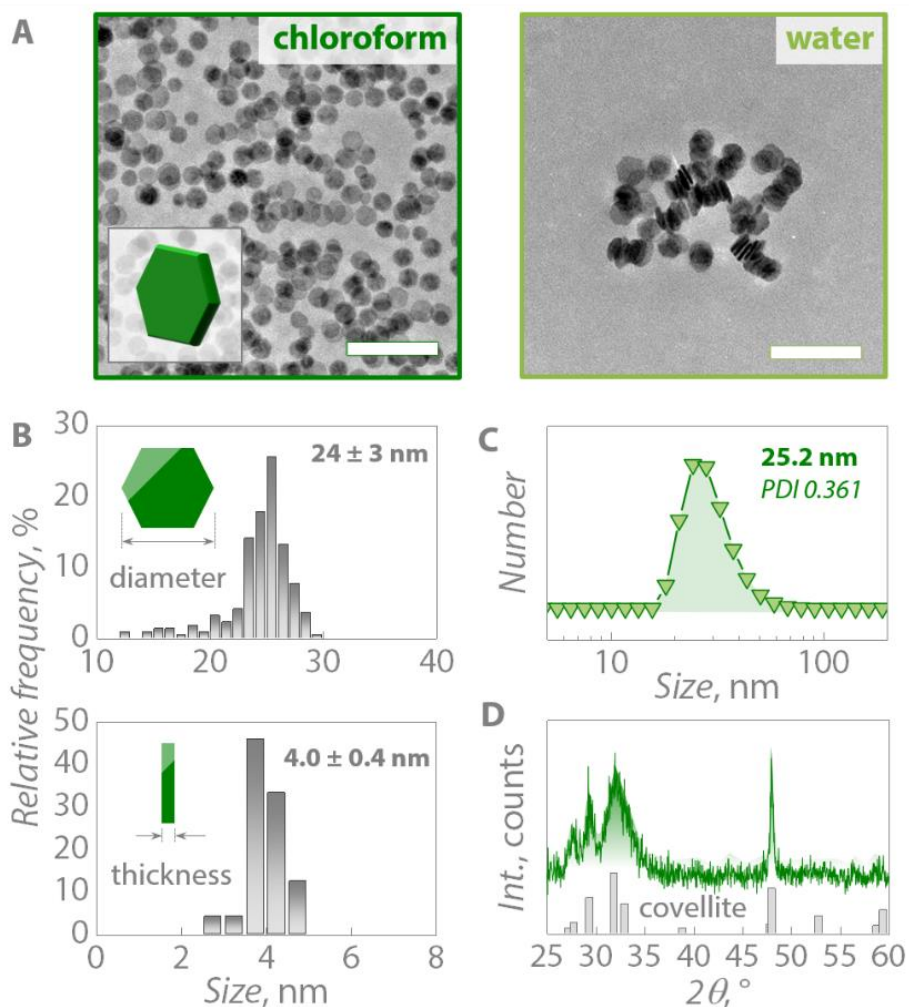[43]   G. Ku, M. Zhou, S. Song, Q. Huang, J. Hazle, C. Li, *ACS Nano* **2012**, *6*, 7489.

Figure 1. A) TEM images of CuS NPs synthesized at 200 °C from Cu(tba)$_2$, capped with OLAm (dispersed in chloroform) and PEG-SH (dispersed in water). Scale bars are 100 nm. B) Geometrical diameter and thickness of the plate-like CuS NPs as obtained from TEM images. C) Results of DLS measurements performed on a phosphate buffer (1x PB) dispersion of PEG-SH-capped CuS NPs. D) X-ray diffraction (XRD) pattern of the CuS NPs compared to reference covellite pattern (PDF card # 01-078-2121).
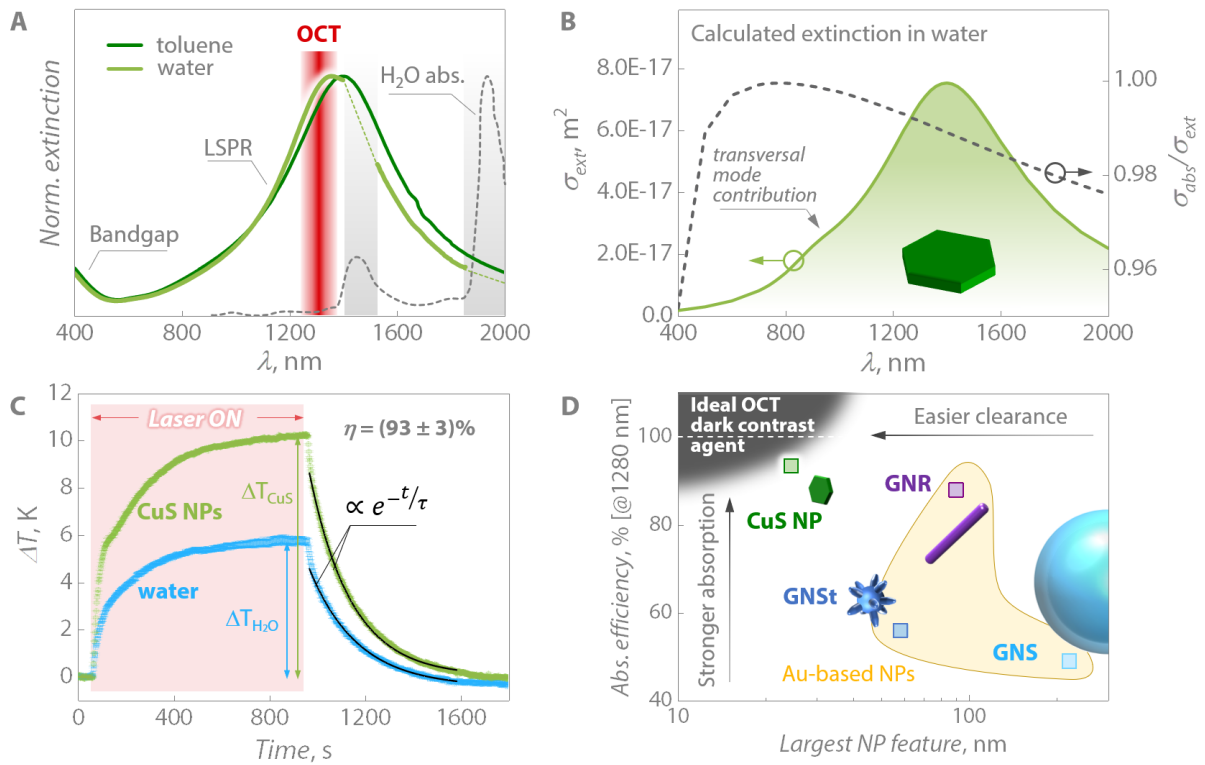
Figure 2. A) Extinction spectra of CuS NPs in toluene (dark green) and in water (light green), respectively before and after exchanging surface OLAm molecules for PEG-SH. Dashed segments in the spectrum of the aqueous dispersion were manually drawn in correspondence of strong water absorption regions. B) Simulated extinction cross section (σ_{ext}) of CuS NPs in water, along with the ratio of absorption (σ_{abs}) over the total extinction (σ_{ext}) that includes both absorption and scattering (σ_{scat}) components. C) Heating-cooling curves obtained from irradiation of water (light blue) and CuS NPs aqueous dispersion (light green) with 1280 nm laser. Black lines in the cooling parts of the curves are single exponential fits to the data. D) Absorption efficiency at 1280 nm (as experimentally calculated) *versus* NP largest feature of plasmonic NPs investigated as OCT contrast agents (GNSt – gold nanostar). The data shown in D was taken from Ref.[18].
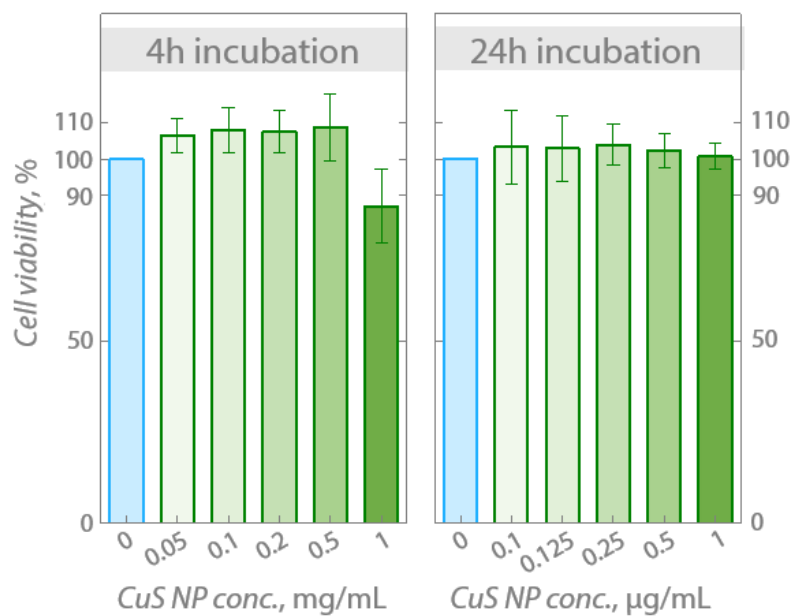
Figure 3. Viability percentage of HeLa cells incubated for 4 and 24 h with dispersions of CuS NPs at different concentrations. Each point corresponds to the mean value (along with its standard deviation) obtained from four different experiments.
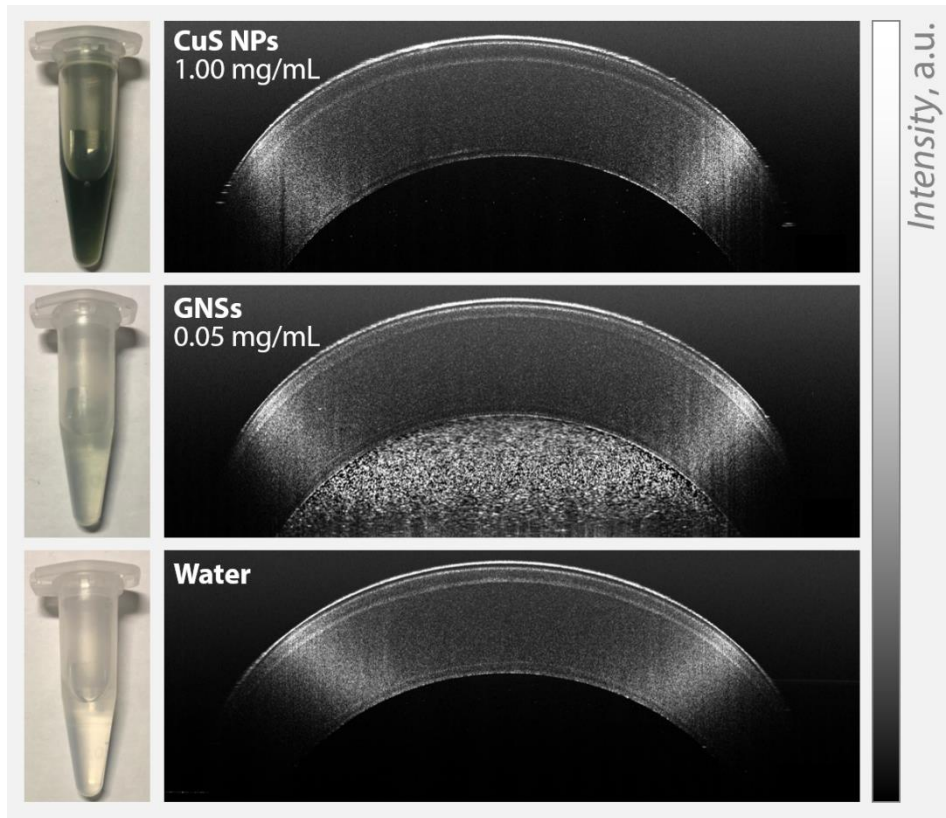
Figure 4. OCT B-scans of Eppendorf tubes containing (from top to bottom): dispersion of CuS NPs in 1x PB, aqueous dispersion of GNSs, water.
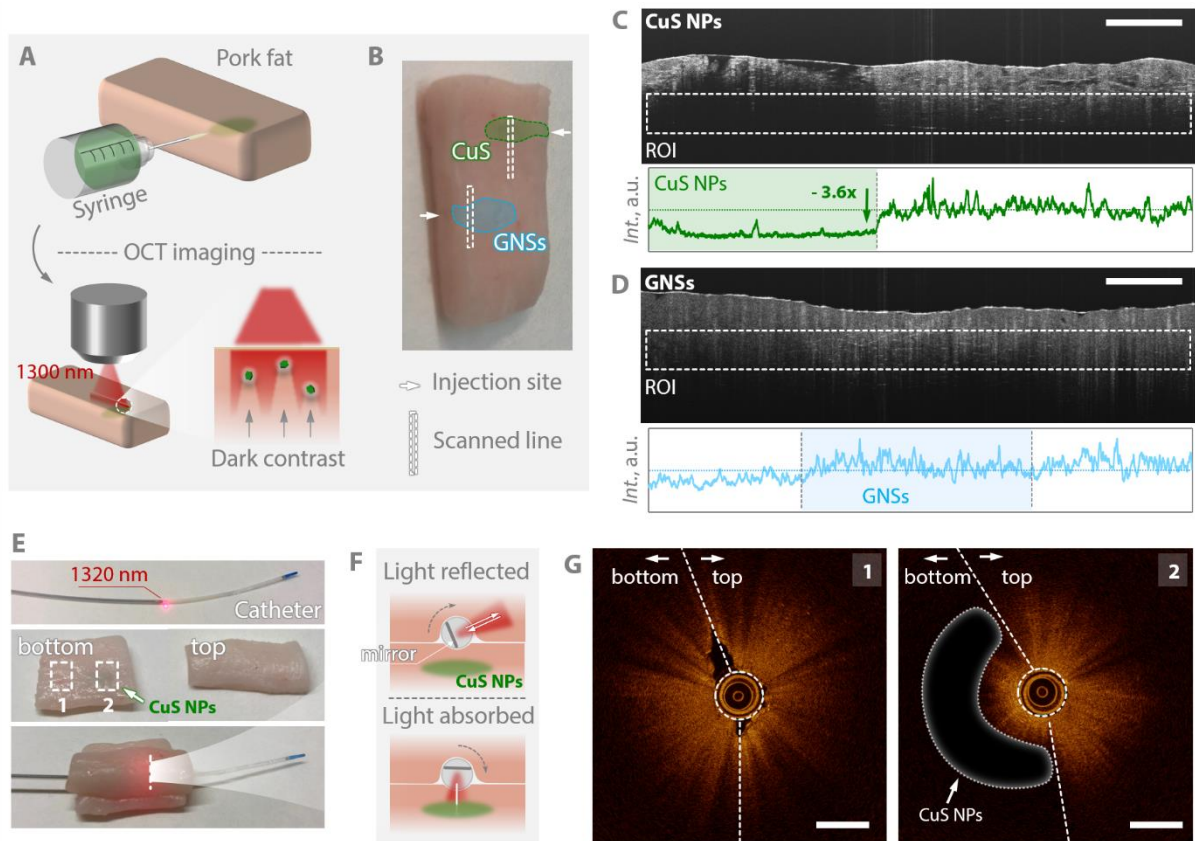
Figure 5. Results of the OCT tests conducted using a SD-OCT instrument (A-D) and an OCT instrument for intravascular imaging (E-G). A) Sketch of the approach employed to test the dark contrast abilities of CuS NPs in pork fat, along with a visualization of the mechanism giving rise to dark contrast. B) Picture of the specimen of the imaged pork fat post injection of CuS NPs and GNSs suspensions. C and D) OCT B-scans obtained in correspondence of the areas where the two types of contrast agents were respectively injected, along with the OCT signal intensity derived from the signal integration on the ROIs indicated in the scans. E) Breakdown of the setup employed for the OCT test using a catheter. The red light observed in the catheter is an idle signal used to indicate where the 1320 nm probing light and the rotating mirror are located. The two rectangles labelled 1 (pristine tissue) and 2 (injected CuS NPs) in the middle picture indicate respectively the areas where the OCT images shown in G were recorded. F) Sketch of section indicated in the bottom picture in E, showing how dark contrast is generated. G) OCT images obtained from the two areas highlighted in E. All scale bars (in C, D, and G) are 1 mm.
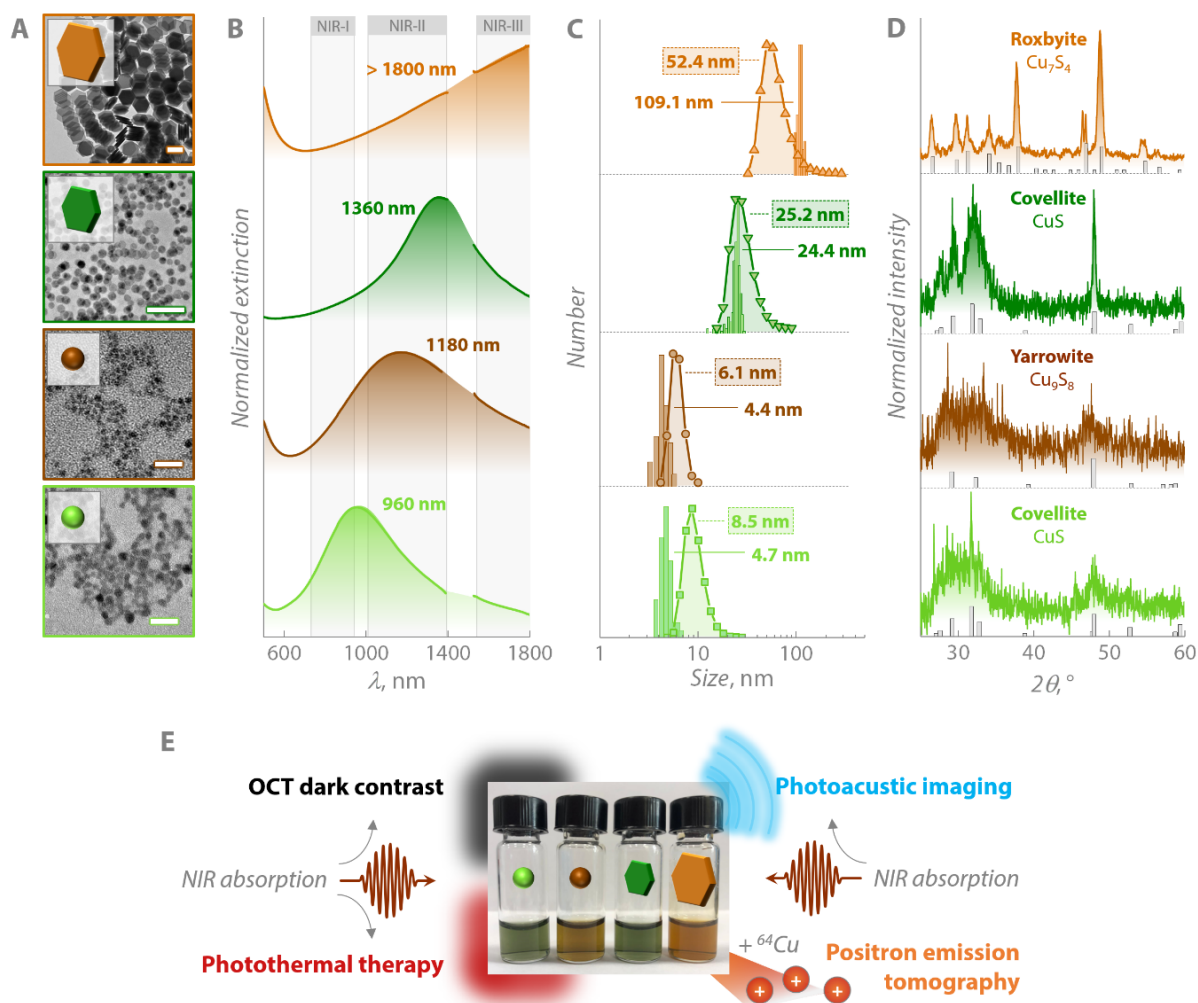
Figure 6. TEM images (A), extinction spectra (B), geometrical and hydrodynamic size (C), and X-ray diffraction patterns (D) of the copper sulfide NPs synthesized in the quest for OCT dark contrast agents. Scale bars in A are 100 and 20 nm for the two top and the two bottom TEM images. In C, the geometrical size reported is the largest NP's feature (i.e., for plate-like particles, the thickness is not reported). The reference patterns in D are taken from PDF # 01-078-2121 (covellite), # 00-036-0379 (yarrowite), # 00-023-0958 (roxbyite). In E, some of the possible applications of copper sulfide NPs in the biomedical context are presented.

Copper sulfide nanoparticles with localized plasmonic resonance in the second optical transparency window were synthesized from thermolysis of copper complexes. The prominent absorption character of their extinction cross section, along with small size and lack of apparent cytotoxicity made them ideal candidates to unprecedently achieve dark contrast in optical coherence tomography.

R. Marin, J. Lifante, L. V. Besteiro, Z. Wang, A. O. Govorov, F. Rivero, F. Alfonso, F. Sanz-Rodríguez and D. Jaque García*

Plasmonic copper sulfide nanoparticles enable dark contrast in optical coherence tomography.
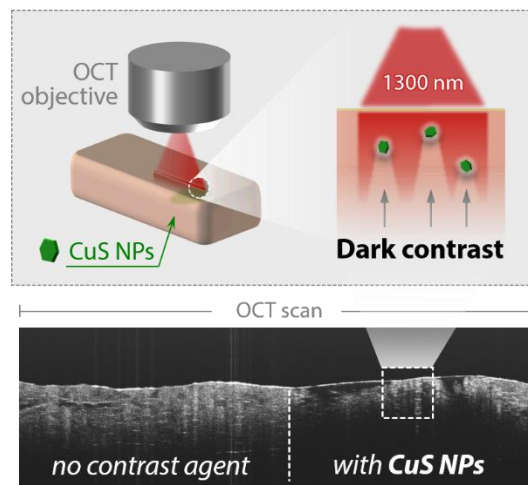
Supporting Information

Plasmonic copper sulfide nanoparticles enable dark contrast in optical coherence tomography.

Riccardo Marin, José Lifante, Lucas Vázquez Besteiro, Zhiming Wang, Alexander O. Govorov, Francisco Sanz-Rodríguez and Daniel Jaque García*

Experimental details

Synthesis of copper sulfide nanoparticles in water. In a typical synthesis of copper sulfide nanoparticles in aqueous environment, 1 mL of a 0.1 M aqueous solution of $Na_2S \cdot 9H_2O$ was swiftly injected into 50 mL of an aqueous solution of the selected ligand and Cu^{2+} (see details in Table S1). After 5 min of stirring at room temperature, the 100-mL round-bottomed flask was transferred to an oil bath pre-heated at 90 °C and the mixture was kept under stirring at that temperature for a total of 1h. During this time, aliquots were sampled, quenched to room temperature and their absorption spectra were recorded (Figure S1). The aliquots selected for further transmission electorn microscopy (TEM) observations were precipitated with isopropanol (iPrOH), recovered by means of centrifugation (30,000 *rcf* for 20 min at 4 °C), and washed once with a mixture of water and iPrOH. The particles were finally stored in de-ionized water (dH₂O).

Table S1. Summary of the experimental conditions (nature and quantity of ligands) used for the synthesis of copper sulfide nanoparticles in water. The pH adjustment was performed using a 0.2 M NaOH solution.

	Ligand	*Ligand amount,* mg [mmol]	*$CuCl_2 \cdot 2H_2O$,* mg [mmol]	*Other notes*
citrate	Na(cit)·2H₂O	17.6 [0.06]	17.0 [0.1]	-
EDTA	H₄EDTA	29.2 [0.1]	17.0 [0.1]	pH adjusted to 9
GSH	L-gluthathione	30.7 [0.1]	17.0 [0.1]	pH adjusted to 9
MHDA	Mercaptohexadecanoic acid	22.6 [0.08]	17.0 [0.1]	pH adjusted to 8
MPA	Mercaptopropionic acid	21.9 [0.2]	17.0 [0.1]	pH adjusted to 9
acac	acetylacetone	20.0 [0.2]	17.0 [0.1]	pH adjusted to 6-7

Synthesis of copper sulfide nanoparticles from CuSCN. The synthesis of these particles was carried out according to a slightly modified, previously reported method.[1] Briefly, 60 mg of CuSCN was added to 10 mL of oleylamine (OLAm) in a 50-mL three-neck round-bottom flask and stirred under vacuum at 100 °C for 30 min. Afterwards, the reaction environment was purged with N_2 and the temperature was risen to 240 °C. Upon reaching the target temperature, the reaction was allowed to proceed for 1 h. Afterwards, the flask was quenched in cold water, the crude product transferred to centrifuge tubes and precipitated upon addition of excess acetone and the particles were collected by means of centrifugation (3,820 *rcf* for 10 min). The particles were re-collected and washed three times with a mixture of toluene and acetone. The particles were finally stored in chloroform. The transfer of these nanoparticles to water *via* ligand replacement (PEG-SH for OLAm molecules) was performed using the same procedure reported for CuS NPs obtained from the thermolysis of $Cu(tba)_2$.
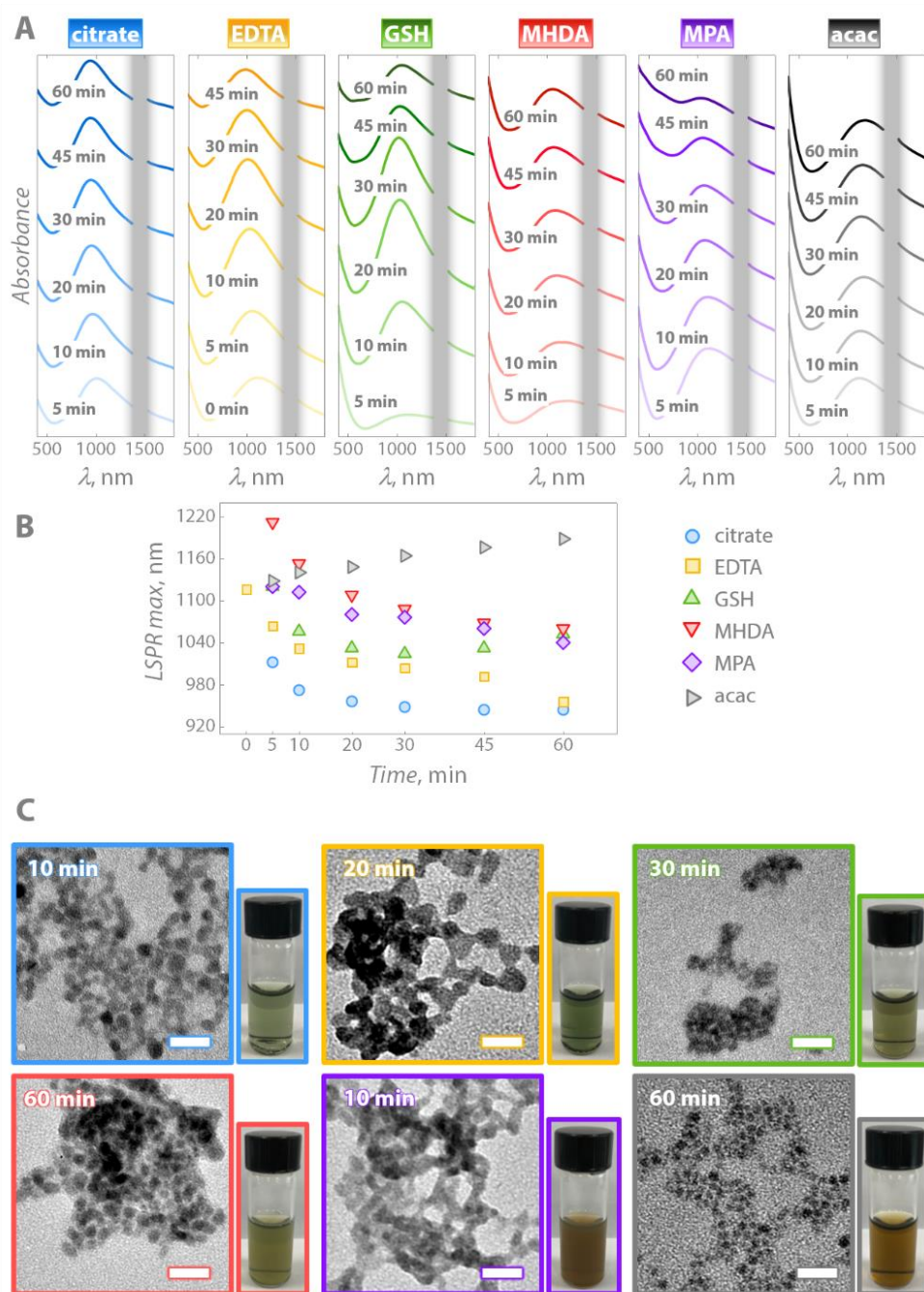
Figure S1. Summary of the properties of the copper sulfide nanoparticles synthesized directly in water. Absorption spectra of aliquots sampled at different time-marks (A), along with the temporal evolution of the localized surface plasmon resonance (LSPR) band maximum (B). TEM images of selected aliquots, along with pictures of corresponding dispersions in water (C).
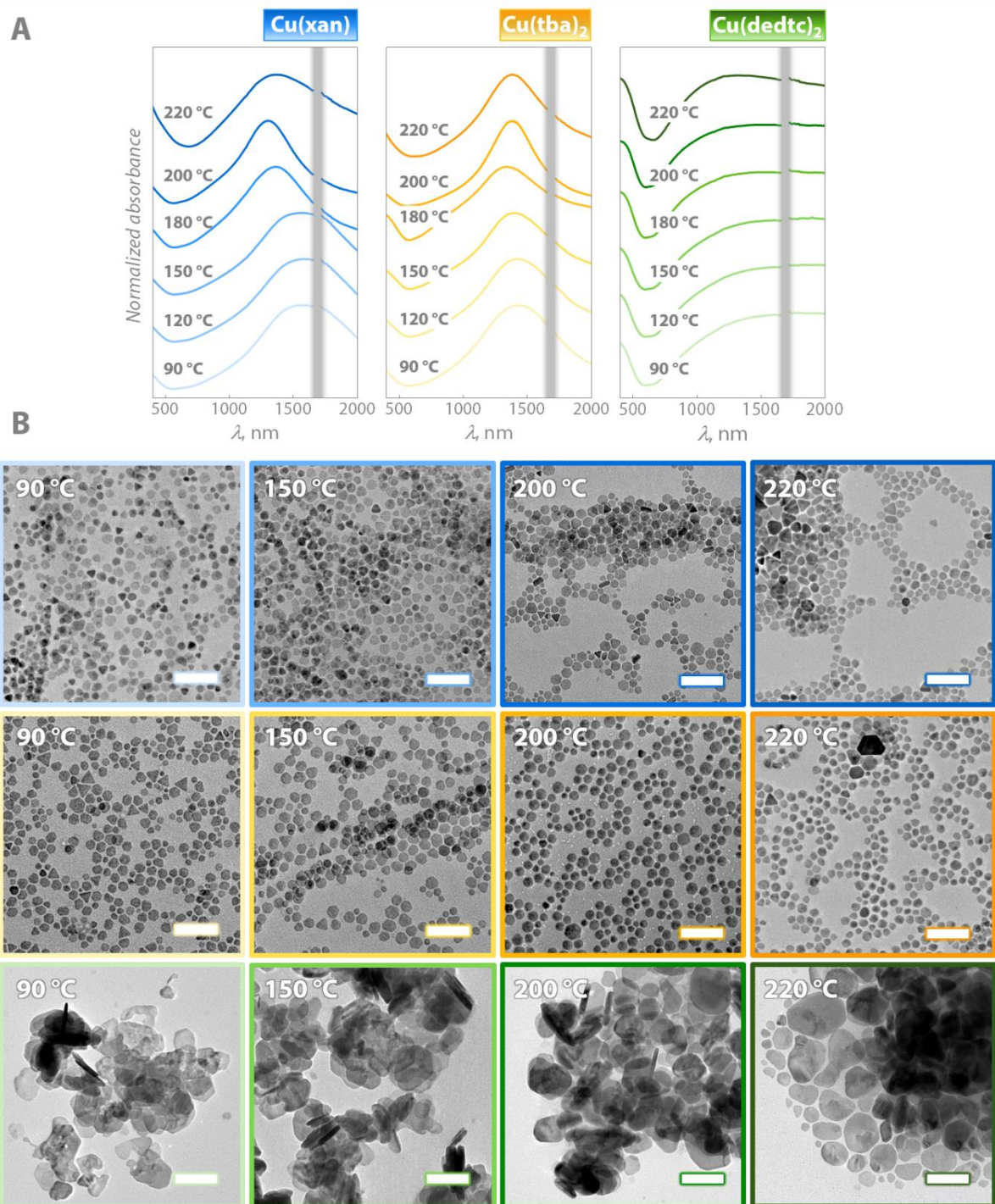
Figure S2. Absorption spectra (A) and TEM images (B) of the copper sulfide nanoparticles synthesized *via* thermolysis of Cu(xan), Cu(tba)$_2$ and Cu(dedtc)$_2$. Absorption spectra were acquired from aliquots sampled at different time-points, quenched in toluene, precipitated with acetone and re-dispersed in toluene. TEM images were acquired only for selected aliquots.
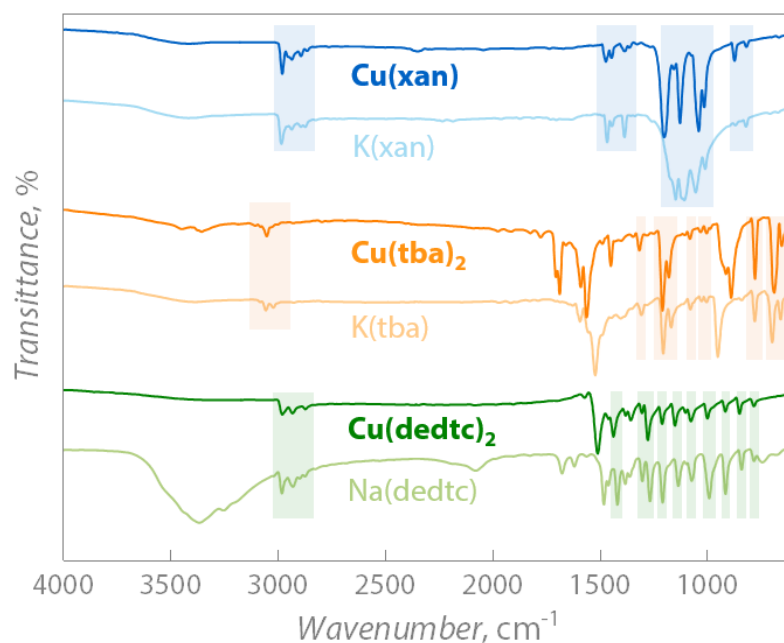
Figure S3. Fourier-transform infrared (FTIR) spectra of the copper complexes used for the preparation of copper sulfide nanoparticles, along with the ones of the corresponding ligands. With colored shaded areas signature signals present in the ligand and in the copper complex are indicated. In Cu(tba)$_2$, some differences can be observed between the signals of the complex and the ligand. The signals in these regions arise mainly from the carboxylic O-H bend (850-950 cm^{-1}), aromatic C-C stretch (1450-1600 cm^{-1}) and the carbonyl group stretch (1650-1700 cm^{-1}). These differences are possibly indicative of some residual moisture in Cu(tba)$_2$, which is also supported the appearance of weak signals just below 3500 cm^{-1}, a difference coordination of the metal to the ligand (either *via* the oxygen or the sulfur atom) and a different stacking of the aromatic moieties. The solution of the crystal structure of this complex lies beyond the scope of the proposed study, hence no further investigation was carried out.
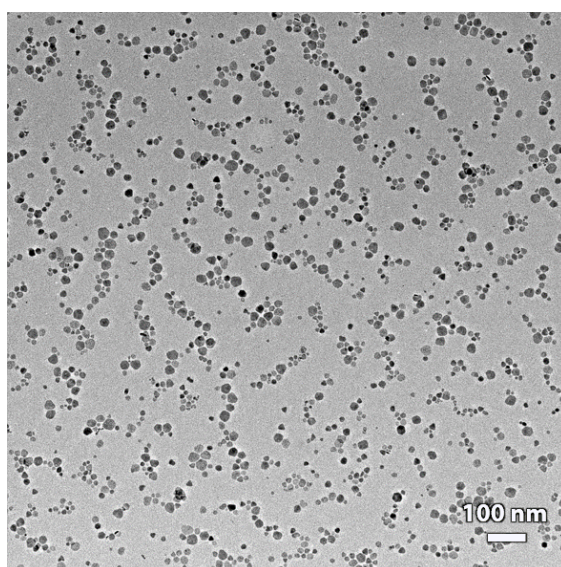

Figure S4. TEM image of copper sulfide nanoparticles obtained upon stirring Cu(tba)$_2$ in OLAm at room temperature for 16 h.

36

Modelling of CuS NPs' electronic properties

The theoretical results presented in the main text and in Figure S5 were obtained with COMSOL Multiphysics, a commercial FEM package used to solve arbitrary systems of differential equations. With it, we calculate the full-wave electrodynamic response of a single isolated CuS nanoplate, immersed in a homogeneous dielectric environment, under continuous wave linearly-polarized illumination. The platelet was modeled attending to the dimensions obtained in the experimental characterization of the sample, and its edges were rounded (with a radius of 0.5 nm) to avoid pathological results arising from unphysically sharp edges.

In order to connect these results with that of a randomly oriented ensemble of nanoplates, relevant for the colloidal suspension studied in the manuscript, we presented in Figure 2B the results averaged over six different combinations of light's incidence and polarization relative to the plate. It is worth noting that the plate supports two main plasmonic modes, one with the polarization of the electric field along its long flat side, and one polarized along its short side (Figure S5).
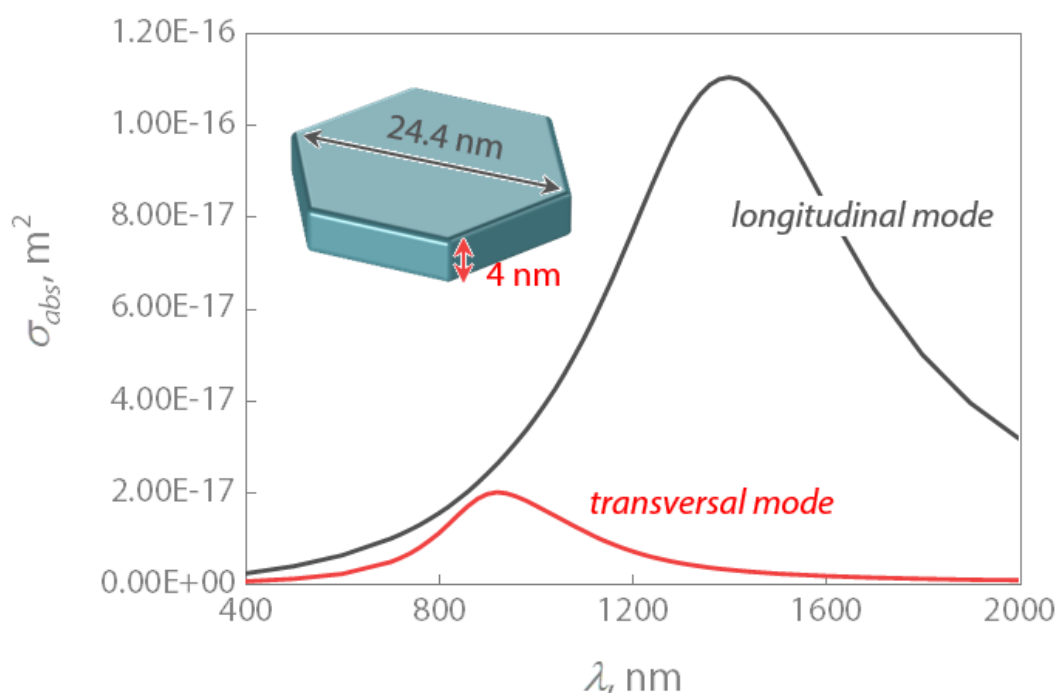

Figure S5. Absorption cross sections for a resonance excited with the electric field polarized along the long side (longitudinal) and along the short side (transversal) of the plate. The inset shows the geometry of the plate and its dimensions in the model. The rounding radius of the corners and edges is 0.5 nm.

The permittivity of the CuS plate was modeled using the Drude model:

$$\varepsilon_{CuS} = \varepsilon_\infty - \frac{\omega_p^2}{\omega(\omega + i\gamma)} \qquad \text{Eq. S1}$$

where ε_∞ is the permittivity at high frequencies, ω_p is the plasma frequency of the material, γ is the damping rate and ω is the angular frequency of the impinging light. The values of these parameters are listed in Table S2. Importantly, the value of the plasma frequency for CuS is estimated from the expected population of carriers supporting the plasmonic charge oscillation, which in this case are the holes in the degenerate semiconductor, as $\omega_p = \sqrt{\frac{e^2 N_h}{m_h \varepsilon_0}}$, where e is the elemental charge, N_h is the hole density, m_h is the reduced mass of the holes and ε_0 is the permittivity of free space. Now, the dielectric constant of the background environment has been estimated for simplicity as the simple average of the dielectric index of the solvent ($\varepsilon_{H_2O} = 1.33^2$) with that of the capping agent ($\varepsilon_{PEG} = 1.455^2$).

Table S2. Parameters describing CuS permittivity, with frequencies expressed in units of energy.[2]

ε_∞	N_h, cm^{-3}	m_h	ω_p, eV	γ, eV
9	10^{22}	$0.8\,m_0$	4.15	0.4

Calculation of the heat conversion efficiency of CuS NPs

The heat conversion efficiency was calculated as reported in the main text (Equation 1), using the experimentally obtained parameters reported in Table S3.

The heat inputs at the numerator were calculated by measuring the temperature T achieved by the system at the thermal equilibrium, through the expression:

$$Q = hA(T - T_{room})$$ \qquad Eq. S2

where T_{room} is room temperature, while hA is the product between the heat transfer coefficient and the area of the sample in contact with the environment, calculated as

$$hA = \frac{mc_p}{\tau}$$ \qquad Eq. S3

where m and c_p are the mass and heat capacity of water and CuS NPs suspension, and τ is the sample time constant, obtained by fitting the cooling part of the heating curves.

The error associated with the final heat conversion efficiency was calculated using standard error propagation, considering the error associated with cooling rate (τ_i) and temperature increase (ΔT_i) of water and CuS NPs suspension, and the impinging laser power (I) reading. The OD was obtained recording the absorption spectrum of the same suspension used for the heat conversion efficiency calculation in a 4-mm optical path cuvette and considering an optical path of approx. 2.62 mm in the case of 0.5 mL of CuS NPs suspension in a 15.6-mm diameter cylindrical well.

Table S3. Summary of the parameters used for the calculation of the heat conversion efficiency. Were applicable, errors on the last digit are given in parentheses.

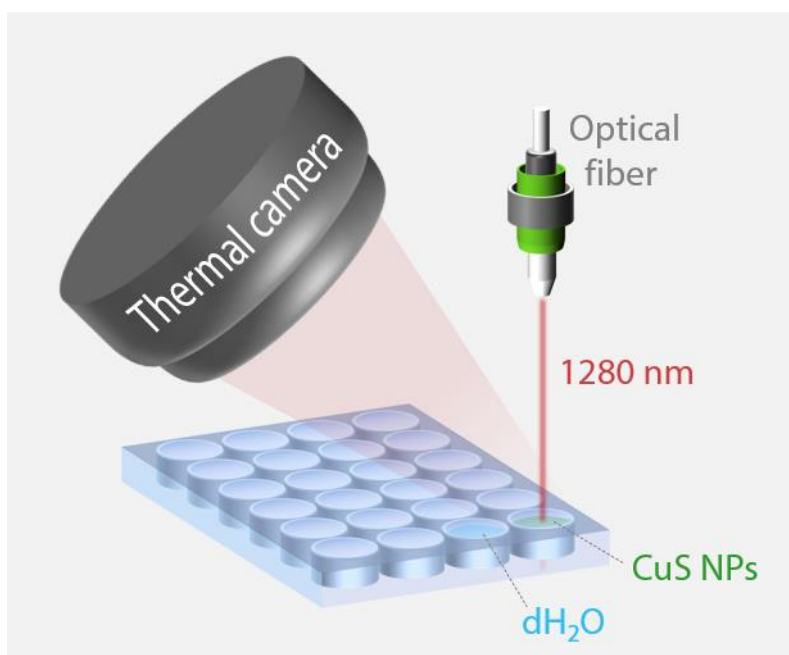|	m, g	c_p, Jg^{-1}K^{-1}	ΔT, K	τ, s	I, mW	OD
CuS NPs	0.5	4.186	10.22(3)	175.0(2)	152(1)	0.252
water	0.5	4.186	5.76(4)	202.2(4)	152(1)	

Figure S6. Sketch of the experimental set-up used for the determination of the heat conversion efficiency (η).

References

1. S. Lee, S. Baek, J. P. Park, J. H. Park, D. Y. Hwang, S. K. Kwak, S.-W. Kim, *Chem. of Mater.* **2016**, *28*, 3337
2. [a] M. R. Kim, H. A. Hafez, X. Chai, L. V. Besteiro, L. Tan, T. Ozaki, A. O. Govorov, R. Izquierdo, D. Ma, *Nanoscale* **2016**, *8*, 12946; [b] R. Marin, A. Skripka, L.V. Besteiro, A. Benayas, Z. Wang, A. O. Govorov, P. Canton, F. Vetrone, *Small* **2018**, *14*, 1803282.